Time-series and moments analysis of atmospheric pressure plasma jet interaction with composite surfaces

V J Law [1,2*] and D P Dowling[2]

[1]Plasma Technology Laboratory, University of Patras, Rio, Greece
[2]School of Mechanical and Materials Engineering, University College Dublin, Belfield, Dublin, Ireland
*(e-mail: viclaw66@gmail.com)

Abstract: A non-invasive off-axis photodiode measurement of an atmospheric pressure plasma jet interaction with aircraft grade composite is reported. The measurement demonstrates a proof-of-concept that the jet nozzle-to-substrate distance can be estimated from the photodiode data, along with the modes of plasma-surface interaction. Namely: Free-space, plasma contact and spreading surface-plasma. A correlation between the photodiode measurements and plasma parameters is found by the use of state-space representation of the modes that employ an embedding delay element that is related to the plasma power supply drive frequency. In addition Pearson r^2 coefficient and third and fourth moment analysis are used to reduce the datasets to a binary code that allows machine control of the plasma process.

1. Introduction

This paper investigates the use of off-axis photodiode measurements as a tool for monitoring an air atmospheric plasma jet. It is well known that when a smooth square waveform, or a time pulse width modulated waveform, is generated, that the time dependent voltage level alternates (within a finite discontinuity) between two voltage levels around an average voltage (V/2). This repeating waveform has symmetry both in time and around the average voltage level. Under these smooth waveform conditions every other even harmonic is suppressed. The even harmonics are missing because of the wave duty-cycle (*D*), which has 50% of the waveform displaced above the zero value of the time axis. Mathematically the duty-cycle may be expressed by equation (1) where *T* is the pulse-on time and *P* is the total time of the wave period which is equal to the reciprocal of the drive frequency (f_o).

$$D = \frac{T}{P}$$

(1)

Without any incorporated signal noise, a simple X-Y orthogonal state-space reconstruction of the one-dimensional (1D) array (t_1, t_2, t_3...) of sampled the data sequence will produce an attractor with ordered pairs at the maximum and minimum values. This simple display couples directly into the human capability to recognise visual images as well allows computer analysis of the 2D pattern. Using these two forms of pattern recognition, it is noted that a sinusoidal waveform would connect the ordered pairs with a line of data points ranging from minimum to maximum. Embedding a delay element (t) on to one of the 1D array (t_m, t_1, t_2, t_3..., where the number (m) is the number of embedding points and depends on the number of sampled points that makeup one period of the waveform [1]. Thus the embedding element will alter the state-space reconstruction of the 2 ordered pairs or add two additional ordered pairs. This is dependent on the equivalent phase difference used: two ordered pairs for 0 or 180 degrees, or 4 ordered pairs when the equivalent phase difference is 90 and 270 degrees. In terms of a Pearson linear regression R-square fit the 0, 180 and 360 degree folded states will exhibit a fit close to 1 along with the unfolded 90 and 270 degree states. A drop in the fitting performance however will occur when chaotic noise amplitude increases with respect to the square waveform amplitude.

Experimentally the square waveform photodiode measurements will have a noise component that is made from timing jitter of the rise and falling edges of the waveform, pulse width modulation and stochastic noise. It is reasonable to assume that under these conditions the number of ordered pairs increase to form clusters. The pattern within each cluster is therefore determined by the equivalent non 0, 90, 180 and 270 phases of the embedded element, and additional noise components will introduce their own deterministic ordered pairs around the clusters: thus the ideal state-space representation of the square waveform is altered. Given this knowledge the deterministic noise may be differentiated and characterised from the coherence of the pure square waveform signal.

Applying this measurement approach to time sampled signals from atmospheric pressure plasma jets is of interest as it is well documented that pulsed and pulse width modulation plasma jets produce both acoustic and modulated polychromic optical emission, both of which are synchronised to the voltage modulation [1, 2 and 3]. In the case of plasma jets operating in unobstructed free-space, the time modulated optical emission is observed to fall in intensity with the gas kinetic temperature along the plasma plume's central axis and extinguishes beyond the visible distal point of the plume [4].

To prevent plasma induced thermal damage [5, 6, and 7] of thermally sensitive materials necessitate that the plasma jet is to be set to a maximum nozzle-to-

surface distance that will achieve the required level of surface activation for a given dwell time. Decreasing the nozzle-to-substrate distance will lead the plasma plume to come into direct contact with the surface and untimely forms a spreading surface-plasma. This will have both spatial and time varying optical intensities due to the formation of irregular filamentary discharge within the afterglow that spreads radially outwards from the plasma contact-point to form a broadly circular reaction zone that is multiples of diameters of the original plasma jet [7]. Thus the coherence of the optical signal emanating from the free-space plasma is deterministically altered as the plasma engages with a surface.

2. Experimental

Atmospheric pressure plasma jet
The atmospheric plasma treatment was carried out using the PlasmaTreat™ Open air atmospheric plasma system [2, 4, 6, and 7]. Figure 1a shows a photograph of the PlasmaTreat™ air plasma jet source used in these experiments and its characteristic temperature regions (arc, flowing afterglow and distal point). This jet system is an example of the blown arc type and uses dry and filtered compressed air as the ionized working gas at a pressure 300 mbar (76.6 l.min^{-1}) through a 5 mm diameter nozzle. The flow of gas produces a force of approximately 6 Newton (6 kg.m.s^{-2}). The plasma jets is electrically driven using pulse width modulated power supply operating at 21 kHz with 80% of the output voltage and a plasma cycle time (PCT) of 80%.

Measurement
To measure the optical emission from the plasma-surface reaction zone, a fixed 45 degree off-axis photodiode measurement was employed. The measurement comprises a collimating lens and optical fibre combination that is focused to a 2 mm volume at the plasma jet central-axis distal point. A Hamamatsu MPPC photodiode with a rise time of 10 ns and spectral range of 320 -900 nm is used to convert the optical signal into an analog signal. A digitizer (-3dB 100 MHz bandwidth) is used to send the digital data at a sample rate of 2 MHz and time-stamped record length of 1500 points to a computer containing a National Instrument LabVIEW program that samples the digital signal.
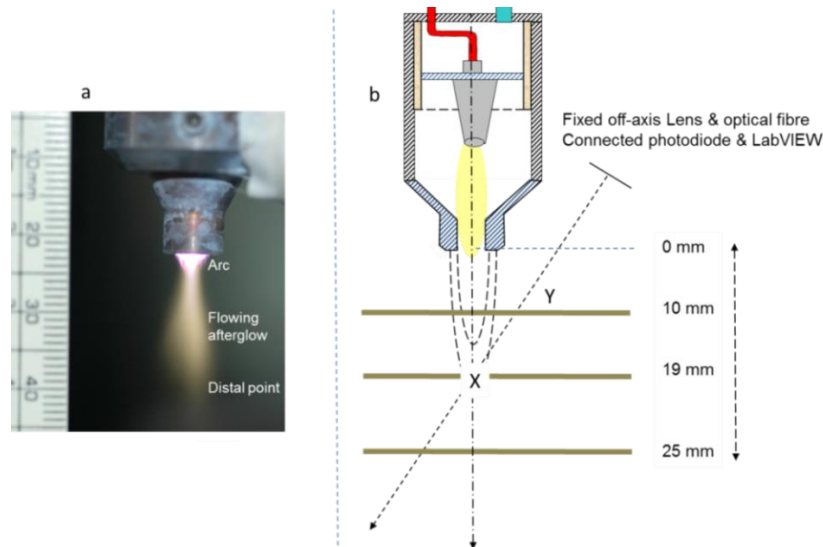
Figure 1ab: Photograph of the PlasmaTreat plasma plume (a); schematic of the off-axis photo diode measurement that is aligned to the distal point with three nozzle-to-surface distances (b). X = distal point and Y is the spreading surface-plasma region.

The purpose of the fixed off-axis position is to allow both the free-space plasma and the surface-plasma to be viewed as the nozzle-to-substrate distance is varied through the plasma jet distal point. Figure 1b shows a schematic of the off-axis photodiode measurement that is focused to the distal point (annotated here as 'X'), three nozzle-to-surface distances (10, 19 and 25 mm). The letter 'Y' denotes the spreading surface-plasma region at 10 mm nozzle-to-surface distance.

Material
The composite is a Hexply® 8552/5H aerospace grade prepreg that consists of 5-harness carbon fibre (AS4) weave pre-impregnated with a non-conductive toughened epoxy resin. The cured composite laminate has a dry glass temperature of $T_g = 200^{\circ}$C [8]. A total of 15 composite test coupons (50 x 25 x 2 mm) were prepared for the plasma treatment. After cutting the edges of these samples were de-burred and then washed in flowing water to remove loose fibres, and finally washed in methanol followed by air jet drying. The coupons are placed on a ceramic surface that is electrical grounded. As the carbon fibre with the matrix of the composite have a typical volume conductivity of 3×10^{-3} Ω.cm and are electrical charged when the plasma jet comes into contact, and the charged leaked to ground through the ceramic.

3. Photodiode measurements
Figure 2 (top) provides a triplet of images of the plasma jet engaging with

aerospace grade composite surfaces as a function of nozzle-to-surface distance (19, 16 and 14 mm), The bottom graph in figure 2 shows 15 photodiode time-traces as the composite surface is moved through the fixed imaging volume.
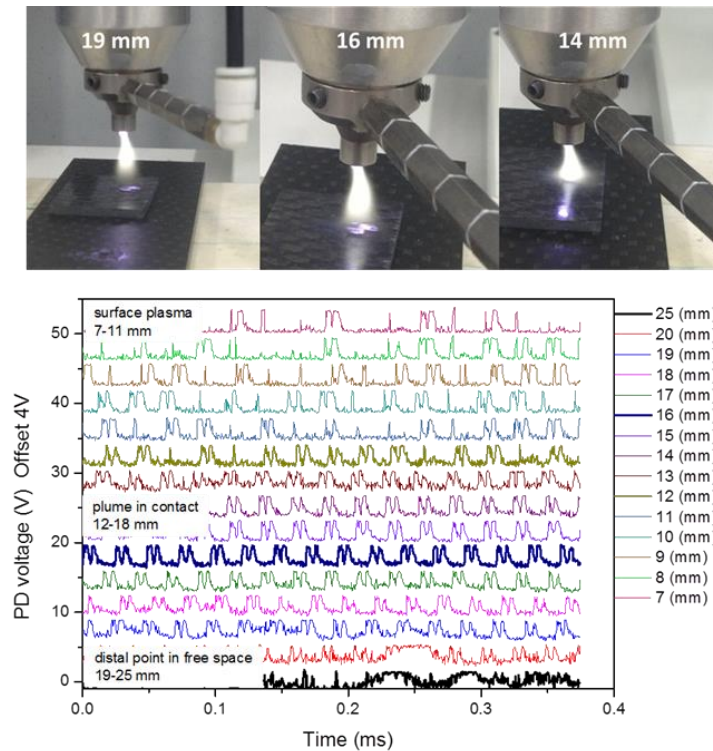
Figure 2 (top) depicting plasma treatment images of the composite at 19, 16 and 14 mm. The bottom graph of figure 2 shows 15 PD time-traces as a function of nozzle-to-substrate distances. The 19, 16 and 8 mm time-traces are highlighted in bold to aid the reader's eye. Distances below 8 mm are not shown as they burn the surface.

The first feature of note in the PD time traces in Figure 2 is that the free-space distal point, plasma-contact and surface-plasma mode have very different time-dependent morphologies. A more detailed polychromic emission analysis reveals that the free-space distal point time-traces exhibit low frequency oscillations, with a periodicity of the order of 0.1 to 0.2 $\times 10^{-3}$s (5 to 10 kHz), with additional pulse timings of 18-21 kHz. As the plasma jet engages with the composite surface from 18 to 12 mm, the 21 kHz, 80 % PCT pulse width modulated drive frequency becomes established. Moving on to the 11 to 7 mm photodiode time-traces that correspond to the spreading plasma-surface mode, the signal become less coherent as some of the drive frequency pulses are missing and replaced with chaotic timing pulses that have bandwidths of 1 to 2 $\times 10^{-6}$s (5 to 10 MHz).

4. Time-series analysis

In this section time-traces that characteristic each of the plasma-surface reaction modes are used. The plasma-contact time-trace is first analysed to establish the second correlation time (τ) [9]: the first correlation time is not used as environmental noise may obscure this this time period. This step is then followed by third and fourth moment analysis. In the second stage the established second correlation time is used to analysis the free-space distal point and the spreading plasma data, followed by moment analysis.

Correlation time stage

The second correlation time step is used to calibrate and establish a standard embedding delay element of the plasma-contact time-traces (12 to 18 mm), in terms of consecutive time-stamped data points that correspond to two periods of the PCT waveform. This standard is then used as a reference to the free-space and spreading surface-plasma modes. For this process the 16 mm time-trace was selected. In the time-domain, the record length ($N = 1500$) is cut into n-frames to obtain the second correlation time. This produce enables each consecutive frame to be overlaid and reveal each quasi-periodic structure to coincide with each other. The sampled data points required to meet the second correlation time is found to be $t_m = 96$. Increasing the frame length further and thereby reducing the number of frames, results in additional t_m to be found: 144, 192, 240, 288, 338, 384, 431... These time sequences correspond to an average frame length of 48 ± 2 data points. As stated previously we use two periods of the plasma power supply drive frequency. Figure 3 shows the 2 periods ($t_m = 96$) where 9 frames of the 96 data points are vertically separated for clarity.

The state-space representation [1, 5 and 10] of the plasma-contact mode is shown in Figure 4a with the embedded data ($t_m = 96$) plotted along the abscissa and the raw data plotted on the ordinate. In this representation the Pearson linear regression (r^2) coefficient = 0.805. Figure 4b is the raw data histogram, where the number of bins is determined using the standard $\sqrt{N}$ criteria, where N = 96, $\sqrt{N} \sim 11$ thus the bin number is set to 11. The third and fourth order moment around the mean analysis [11] of the datasets reveals a probability distribution profile with a Skewness = 0.8, where a value of 0 represents a normal distribution, and a Kurtosis component = 2.04 which indicates the distribution profile has a peak near the mean value.

.
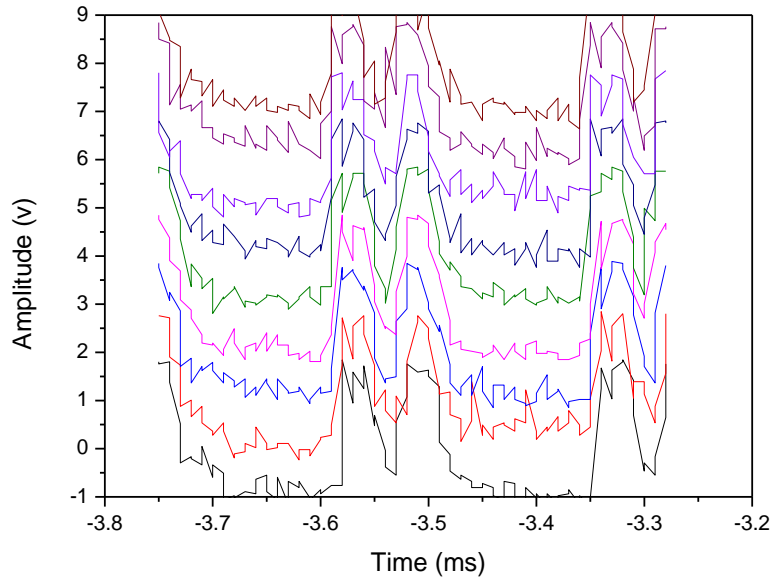
Figure 3: 2 period calibration of correlation time for the plasma contact mode: 16 mm time trace and an embedding element $t_m = 96$.
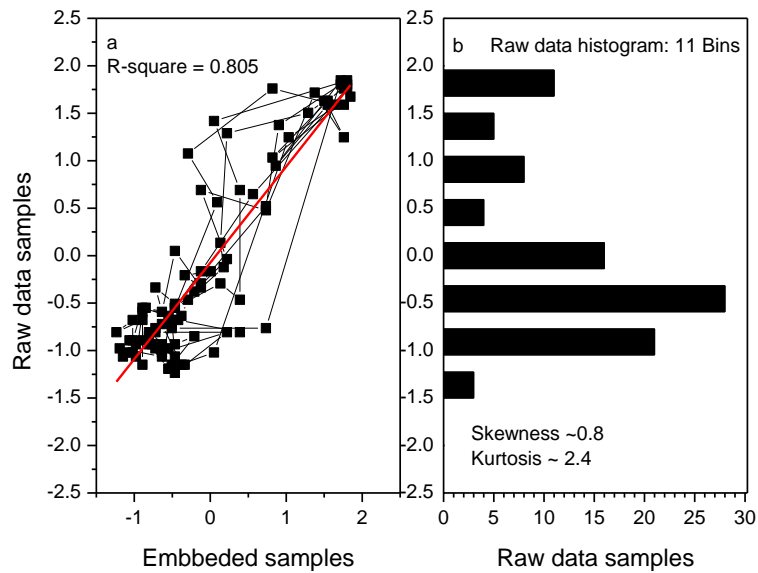
Figure 4: Calibration for plasma-contact mode: 16 mm time-trace. State-space representation with $t_m = 96$ (a) and raw data histogram (b).

Second stage of embedding

The second stage of the embedding delay process now proceeds with the free-space and spreading plasma-surfaces 1D arrays for the same value of t_m = 96. The results are shown in figure 5 (Free-space distal point) and Figure 6 the spreading surface-plasma. With this knowledge it is possible to compare the cluster and trajectory of individual data points for all three plasma reactions modes.

Figure 5a shows the Free-space state-space representation of free-space delay pot along with the associated r^2 value (0.395). In this case the display reveals a single cluster of 96 data points positioned between 1.5 and -1.5 on the ordinate scale (5 outliners are positioned beyond the 2.5 scale on the abscissa). The probability distribution profile of the raw data in Figure 5b reveals a Skewness = -0.28 and a Kurtosis component = 2, both of which indicate a broad, but non, Gaussian distribution profile with a. The low value of r^2 combined with broad non-Gaussian profile indicates a complex structure within the data. Using this form of descriptive analysis it is reasonable conjecture that this morphology is the result the rapidly cooling plasma jet gas kinetic temperature that is free to mix with the surrounding air. It should be noted that stepwise increasing the number data points used in higher order t_m embedding nodes does not alter the cluster structure, only the geometric centre of the cluster is moved around the zero value of abscissa and ordinate.
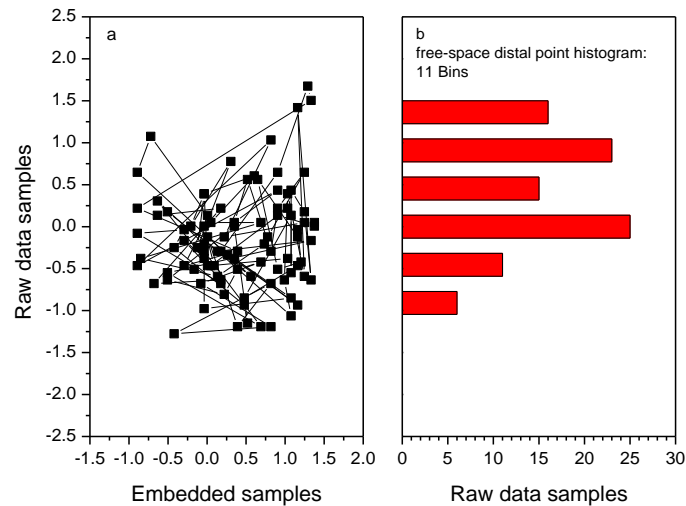
Figure 5ab: Free-space distal point mode: 25 mm time-trace. State-space representation with t_m = 96 (a) and raw data histogram (b).

Moving on to the spreading surface-plasma mode (8 mm) the state-space representation (Figure 6a) reveals a main cluster with what appears to be at least

two other clusters. The r^2 coefficient for the complete dataset = 0.587 which again is much lower than the plasma-contact mode. However caution in the use of this test must be used due to the additional two clusters. A detailed examination of the data reveals a multimodal distribution with a major cluster of 65 out of the 96 data points formed in the X-Y negative quadrant of the plot and two trajectories. The first trajectory bisects the abscissa and ordinate with the similar vector as the plasma-contact mode with a total of 17 data points, 7 of which are above scale value of 2 on the embedded axis. This number of data points and trajectory can be mapped to features in the PCT waveform. The second trajectory is perpendicular to the abscissa with 2 data points above the scale value of 1 on the ordinate. Mapping back to the original dataset these trajectory have the same chaotic time scales as the optical intense and irregular filamentary formations within the surface plasma glow. The moment analysis of the raw data (Figure 6b) reveals a bimodal distribution with a Skewness = 1.54 and a Kurtosis component = 5.97.
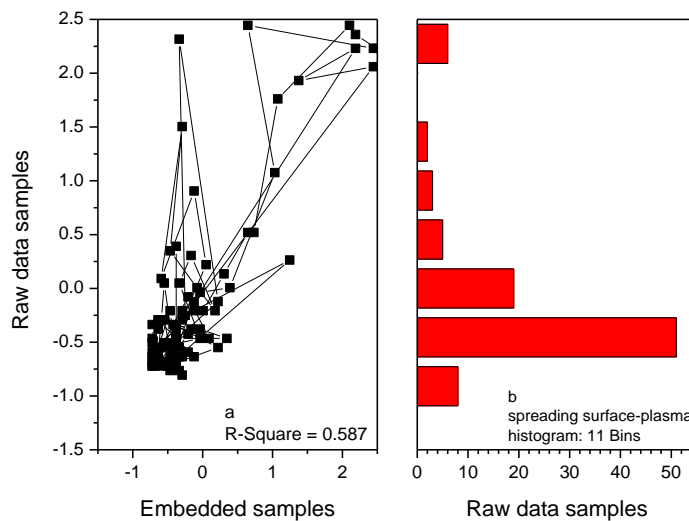
Figure 6ab: Spreading surface-plasma mode: 8 mm time-trace State-space representation with t_m = 96 (a) and raw data histogram (b).

5. Moment analysis over extended values of frame length and t_m

It must be stated the third order of moment around the mean (Skewness) needs carful interpretation because zero Skewness does not mean to imply the mean is equal to the median, as in the case of discrete distributions that are multimodal or have a significant fourth order of moment (Kurtosis) around the mean. Given this corollary, Skewness and Kurtosis may be used as supportive evidence when used as a diagnostic tool, similar to the acoustic moment analysis reported in reference [10]. Therefore in this section the frame length of the raw data Skewness and Kurtosis (table 1) are compared with a limited range of

equivalent embedded values (table 2).

Table 1 shows the Skewness and Kurtosis values of the raw data (frame length = 96), for all three nozzle-to-surface distances. Here it can be seen that the individual values exhibit a clear separation between each of the plasma modes. When compared to the moment values for t_m = 96, 144, 192, 240 and 288 in table 2 there is a degree of overlap in the spread (minimum to maximum) between the nozzle-to-surface distances 0f 16 and 25 mm datasets, which would indicate a connection between the plasma modes; whereas there is no overlap between the 8 and 26 mm datasets. This overlapping and non-overlapping observation may provide a degree of classification usefulness when coupled with the r^2 test.

Table 1: Skewness and Kurtosis values for raw data as a function of frame length and nozzle-to-surface distance.

Frame length	Nozzle-to-surface distance		
	8 mm	16 mm	25 mm
96	1.9	0.80	-0.25
	5.7	2.04	1.93

Table 2: Skewness and Kurtosis values as a function of *m* and nozzle-to-surface distance.

(t_m)	Nozzle-to-surface distance		
	8 mm	16 mm	25 mm
96	1.92	0.78	-0.26
	5.97	2.04	1.99
144	0.90	0.78	0.62
	2.23	2.03	2.66
192	1.13	0.69	1.03
	2.74	1.86	4.21
240	1.84	0.63	0.73
	5.27	1.74	3.18
288	1.37	0.66	0.10
	3.31	1.80	1.64
Minimum -	0.9 to 1.92	0.63 to 0.78	-0.26 to 1.03
maximum	2.23 to 5.75	1.74 to 2.04	1.64 to 4.21

6. Machine control

In this section the transformation of the 2D state-space information to a binary code is considered as a means of machine control [12]. The result of the r^2 test for a limited t_m range (84 to 108) is shown in figure 7 for each plasma mode.
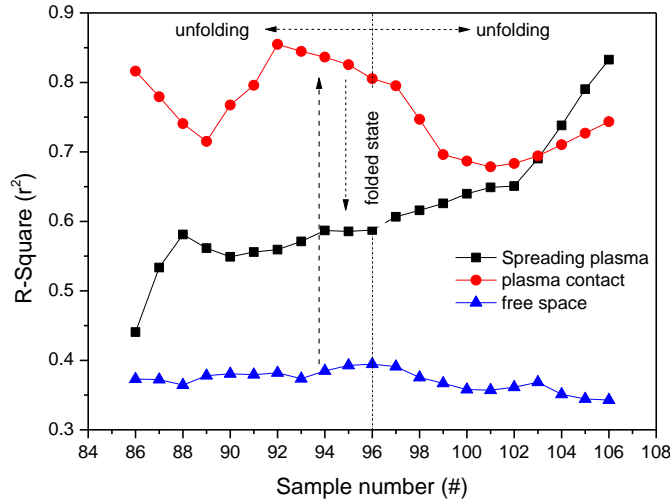
Figure 7: r^2 coefficient as a function of t_m (84 to 108) for each plasma mode.

In this figure it can be seen that the Free space mode exhibits little variation in: r^2 (0.35 to 0.4) due to near Gaussian distribution profile of the data points. As the plasma engages with the composite surface electrical is made and the photodiode time trace takes on a repeating quasi-square waveform structure. In this plasma mode varying tm from 84 to 108 around the reference embedding number of 96 yields a slow sinusoidal profile within the r^2 coefficient limits of 0.7 to 0.85 where the slow wave is due to the phase difference between the quasi-square wave raw data and the embedded data. However as the plasma engages further with the composite the r^2 coefficient undergoes a pronounced change in trace profile, from $r^2 = 0.4$ at $t_m = 84$ to 0.8 at $t_m = 108$. Under this Spreading plasm mode varying tm conditions reveals the spatial-temporal nature of the surface filaments. This last mode demonstrates then need to maintain t_m at, or at least very close to, a set number periods of the plasma power supply drive frequency.

Given the PD measurements described here and the form of data analysis it is possible to define a simple protocol for machine control of the plasma-composite gap height. The limits for each mode are set out in table 3. In this table the r^2 coefficient for the spreading plasma was further investigated and yielded a range of 0.55 to 0.65 for $t_m = 48$, 96,144.1992, 240 and 288. Thus the experimental define ranges for each test may be used to characterise the plasma-surface interaction mode.

Table 3: r^2, Skewness and Kurtosis limits for each plasma mode.

Test	Free-space	Plasma contact	Spreading plasma
r^2	0.35 to 0.4	0.7 to 0.85	0.55 to 0.65
Skewness	-0.26 to 1.03	0.63 to 0.8	0.9 to 1.92
Kurtosis	1.64 to 4.21	1.74 to 2.04	2.23 to 5.74

7. Summary and future work

A non-invasive off-axis photodiode measurement approach for monitoring the interaction of an air atmospheric pressure plasma jet with a conducting aerospace composite surface is presented. Probability distribution profiles of raw data in conjunction with embedded state-space representation identifiers the nozzle-to-surface distance and the associated plasma surface interaction mode (free-space distal point, plasma-contact and spreading surface-plasma). In the case of the spreading surface-plasma mode third and fourth order moment analysis of the raw data does provide identification of the optically intense and irregular filamentary formation, thereby providing an additional supportive means to visual identification and classification of the mode.

Currently, the state-space reconstructions, R^2 test and moment analysis are performed off-line. In the future the combination of the measurements and tests on real-time measurements may provide a means of machine control. As the measurement is non-invasive (no electrical connection to the plasma system is required) retrofitting to other plasma jet systems can be made.

Before this ultimate goal is achieved further study of the initial unfolding process as $t_m \to 0$ is required to define region between a monitoring process and a real-time control systems that does not produce false positive results. An additional line of research would be to apply the measurements to rotating plasma nozzles [13] and the delineation between different non conducting surfaces and conducting surfaces.

References

[1]   Three distinct modes in a cold atmospheric pressure plasma jet J L Walsh, F. Iza, N B Janson, V J Law and M G Kong. J, Phys, D: Appl, Phys. 43(7), 075201 (14pp), 2010

[2]   Evaluation of the sensitivity of electro-acoustic measurements for process monitoring and control of an atmospheric pressure plasma jet system. V J Law, F T O'Neill and D P Dowling. Plasma Sources Sci, Technol. 20(3), 035024, 2011.

[3]   Resonances and patterns within the atmospheric pressure plasma jet kINPen-med. V J Law, A. Chebbi, F T O'Neill and D P Dowling. CMSIM Journal. 1: 3-10, 2014.

[4]   DC pulsed atmospheric pressure plasma jet image information. D P Dowling, F T O'Neill, V Milosavljević and V J Law. IEEE Trans, Plasma Science. 39(11), 2326-2327, 2011.

[5]   Active control metrology for preventing induced thermal damage during atmospheric pressure plasma processing of thermal sensitive materials. V J Law and D P Dowling. ISCS 2013: International Symposium on Complex Systems. Emergence of Complexity and Computation, Vol. 8 chap 32 pp, 321-332. Eds: A, Sanyei, I, Zelinka, O, Rossier. (Springer-

Verlag, Berlin Heidelberg) 2014. ISBN: 978-3-642-45437-0

[6]   The importance of plasma thermal energy transfer for plasma jet systems. D P Dowling, *et al*. IEEE Plasma Science 40(10), 2426-2427, 2014.

[7]   Air-based atmospheric pressure plasma jet removal of FreKote 710-NC prior to composite-to-composite bonding. V J Law, J Mohan, F T O'Neill, A Ivankovic, and D P Dowling. Int, J, Adhesion and Adhesives. 54(C), 72-81, 2014.

[8]   Information on the Hexply material can be found at http://www.hexcel.com

[9]   Using average mutual information to preview the power spectrum and to guide nonlinear noise reduction. N Jevtic, W Nilsen, P Stine, J S Schweitzer. CMSIM Journal. 1: 187-197, 2011.

[10]   Experimental and theoretical investigation of dielectric-barrier plasma jet in helium. I Topala, N Dumitrascu, and D-G Dimitru. IEEE Trans, Plasma Science. 40(11) 281-2816, 2012.

[11]   Atmospheric pressure plasma acoustic moment analysis. V J Law, N T O'Neill, D P Dowling. Complex Systems 20(2), 181-193, (*Complex Systems, Publications, Inc 2011*).

[12]   Visualization of a dual frequency plasma etch process. V J Law. N Macgearailt. Meas, Sci, Technol. 18(3), 645-649, 2007.

[13]   Influence of rotating electrode on the uniformity of atmospheric pressure air filamentary barrier discharge. D Yu, *et al*. Plasma process, Polym, 10(10), 880-887, 2013.